(article starts on next page)

Impact of Anisotropic Cosmic-Ray Transport on the Gamma-Ray Signatures in the Galactic Center

J. Dörner[1,2] , J. Becker Tjus[1,2,3] , P. S. Blomenkamp[2,4] , H. Fichtner[1,2] , A. Franckowiak[2,4] , and E. M. Zaninger[1,2]
[1] Theoretische Physik IV, Fakultät für Physik & Astronomie, Ruhr-Universität Bochum, 44780 Bochum, Germany
[2] Ruhr Astroparticle and Plasma Physics Center (RAPP Center), Ruhr-Universität Bochum, 44780 Bochum, Germany
[3] Department of Space, Earth and Environment, Chalmers University of Technology, 412 96 Gothenburg, Sweden
[4] Astronomisches Institut, Fakultät für Physik & Astronomie, Ruhr-Universität Bochum, 44780 Bochum, Germany

Abstract

The very high energy (VHE) emission of the central molecular zone (CMZ) is rarely modeled in 3D. Most approaches describe the morphology in 1D or simplify the diffusion to the isotropic case. In this work, we show the impact of a realistic 3D magnetic field configuration and gas distribution on the VHE γ-ray distribution of the CMZ. We solve the 3D cosmic-ray transport equation with an anisotropic diffusion tensor using the approach of stochastic differential equations as implemented in the CRPropa framework. We test two different source distributions for five different anisotropies of the diffusion tensor, covering the range of effectively fieldline-parallel diffusion to isotropic diffusion. Within the tested magnetic field configuration, the anisotropy of the diffusion tensor is close to the isotropic case, and three point sources within the CMZ are favored. Future missions such as the upcoming CTA will reveal more small-scale structures that are not yet included in the model. Therefore, a more detailed 3D gas distribution and magnetic field structure will be needed.

Unified Astronomy Thesaurus concepts: Galactic cosmic rays (567); Galactic center (565); Gamma-rays (637)

1. Introduction

The Galactic center (GC) is one of the most extreme and close-by astrophysical environments and is of particular interest for studies of nonthermal processes. The GC has been studied in all wavelengths from the radio (Heywood et al. 2022) to high- (Ajello et al. 2016; Di Mauro 2021) and very high energy (VHE) γ-rays (Abramowski et al. 2016; Abdalla et al. 2018; Acciari et al. 2020; Adams et al. 2021). The observed outflows at γ-ray (Ackermann et al. 2014), X-ray (Sofue 2000), microwave (Finkbeiner 2004; Planck Collaboration et al. 2013), and radio wavelengths (Pedlar et al. 1989) as well as small-scale structures such as nonthermal filaments and molecular clouds (see Henshaw et al. 2023, for a review) are in need of proper modeling.

The observation of VHE γ-rays, which were first reported by the High Energy Stereoscopic System (H.E.S.S.; Abramowski et al. 2016), indicates the acceleration of cosmic-ray (CR) protons up to PeV energies. The GC is one of a few so-called PeVatrons known in our Milky Way. The diffuse VHE γ-ray emission in the GC has been spatially correlated with the dense gas of the central molecular zone (CMZ) and seems to be consistent with the injection of CRs by a steady-state source located at the GC (Abdalla et al. 2018). In Abramowski et al (2016) and Abdalla et al. (2018), the projected distribution of the H_2 column density inferred by the observation of the CS(1-0) line multiplied by a parameterized source profile of a Gaussian or a $1/r$-CR density profile was used. This approach of modeling the CR transport neglects the existence of small-scale features in the 3D gas distribution as well as in the magnetic field.

The first attempt to model the γ-ray emission of the CMZ using a 3D gas distribution was carried out by Scherer et al.

(2022). These authors probed whether the gas had an inner cavity. In lack of a 3D magnetic field, the authors assumed isotropic diffusion for a Kraichnan spectrum of magnetic turbulence. Recently, these authors tested more realistic source distributions and a two-zone diffusion model (Scherer et al. 2023).

In this paper, we use the results of Guenduez et al. (2020) in order to perform diffusive 3D CR propagation in the CMZ. We include the 3D gas distribution for interactions and distinguish between parallel and perpendicular diffusion. Further, we test different source-injection models that are related to point sources inside the CMZ and a sea of Galactic CRs.

The paper is organized as follows: in Section 2, the GC environment and its observations are summarized. In Section 3, the transport model and simulation setup are presented, and in Section 4 the simulation results are compared to the observed data. Finally, in Section 5, a concluding discussion and an outlook are given.

2. Galactic Center Environment

2.1. VHE γ-Ray Observation

The GC has been studied in VHE γ-rays ($>$100 GeV). The first detection of $\sim$100 TeV γ-ray emission by Abramowski et al. (2016) provided the first evidence for the existence of a PeVatron in the GC region. In Abdalla et al. (2018), H.E.S.S. quantified the spatial distribution of the diffuse γ-rays and the corresponding spectrum. Even MAGIC (Acciari et al. 2020) and VERITAS (Adams et al. 2021) have observed the CMZ. High-energy γ-ray emission from the GC has been detected at GeV energies by FermiLAT. As the GC region shows deviations from the typical expectation of CR transport (Ackermann et al. 2017), dark matter has been proposed to be a possible contributor at GeV energies (Goodenough & Hooper 2009; Daylan et al. 2016).
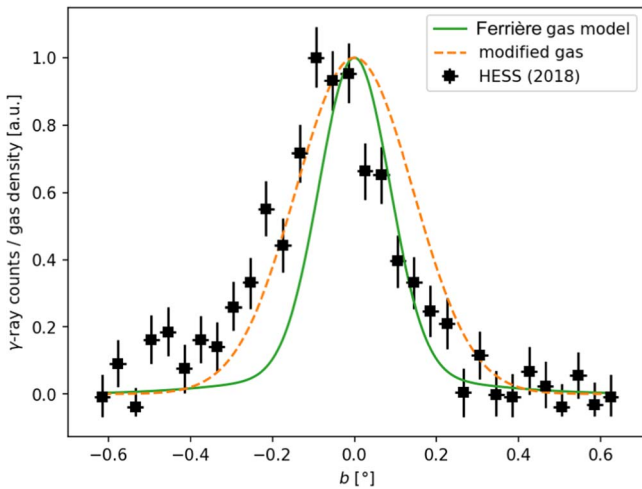
Figure 1. Comparison between the latitudinal profile (b) of the observed diffuse γ-ray flux (black squares) by H.E.S.S. (Abdalla et al. 2018) and model of the gas distribution (solid green line) by Ferrière et al. (2007). The dashed orange line corresponds to the gas distribution using a larger parameter for the scale height of $H_c = 30$ pc.

At >100 TeV γ-ray energies, LHASSO has reported the detection of photons from the Galactic plane (Cao et al. 2023). The IceCube collaboration also reported the first observation of the Galactic plane in high-energy neutrinos, which represents unambiguous proof of the signatures of hadronic CRs (Abbasi et al. 2023). At this point, the exact contribution to the Galactic emission from the GC region cannot be quantified from the observational perspective. Theoretical studies like this paper can help to understand whether a significant fraction of the total neutrino flux comes from the diffuse emission of the GC, and we quantify the number of neutrinos that can be expected to come from the central diffuse part in this study.

2.2. Gas Distribution

The 3D gas distribution of the CMZ is not well known, and the models are quite uncertain. We use the HI and H_2 CMZ components of the model by Ferrière et al. (2007). It is parameterized as

$$n(\mathbf{r}) = n_0 \exp\left\{-\left(\frac{\sqrt{X^2 + (2.5Y)^2} - X_c}{L_c}\right)^4\right\}$$
$$\times \exp\left\{-\left(\frac{z}{H_c}\right)^2\right\}, \quad (1)$$

where X and Y are the local coordinates along the major or minor axis.

In contrast to the observed latitudinal profile of the diffuse γ-ray emission, the gas model shows a significantly shorter scale height of the disk (see Figure 1). The maximum width of the latitudinal γ-ray profile independently of the transport mechanism is determined by the gas distribution, and the distribution suggested by Ferrière et al. (2007) cannot explain the observations. Therefore, we adjust the scale height of the gas distribution to $H_c = 30$ pc, which is near the upper limit of the observational uncertainties. With these changes, a reproduction of the latitudinal profile is possible (see Section 4.2 and Figure 5).

2.3. Magnetic Field Configuration

To determine the local directions of parallel and perpendicular CR transport, the knowledge of the 3D magnetic field configuration is crucial. Here, we use the model proposed by Guenduez et al. (2020), which is a superposition of a large-scale intercloud (IC) component and more localized contributions. These small-scale components include the eight observed nonthermal filaments (NTF), 12 molecular clouds (MC), and a contribution from Sgr A*. The IC and NTF components are predominantly poloidal, while the molecular clouds are toroidal. In the MCs, the ratio $\eta = B_r/B_\phi$ of the radial and azimuthal field is fixed to $\eta = 0.5$, as suggested in Guenduez et al. (2020). The total magnetic field can be written as

$$\mathbf{B}_{\text{tot}} = \mathbf{B}_{\text{IC}} + \sum_{i=1}^{8} \mathbf{B}_{\text{NTF},i} + \sum_{i=1}^{12} \mathbf{B}_{\text{MC},i} + \mathbf{B}_{\text{SgrA*}}. \quad (2)$$

In Figure 2, a superposition of the magnetic field structure and the projected column density is given. In general, the transport of CRs is determined by the IC component of the magnetic field. To confine CRs and for the local enhancement of γ-ray emission, the magnetic cloud sgr B2, the field around Sgr A*, and the NTF radio arc are most important. These structures are indicated in Figure 3 in cyan.

3. Simulation Setup

The transport of Galactic CRs can be described by the Parker equation (see, e.g., Becker Tjus & Merten 2020),

$$\frac{\partial n}{\partial t} = \nabla \hat{\kappa} \nabla n - \frac{\partial}{\partial E}\left[\frac{dE}{dt}n\right] + S(\mathbf{r}, E, t), \quad (3)$$

where $n = n(\mathbf{r}, E, t)$ denotes the differential number density of CRs per unit volume, energy, and time. The diffusion tensor $\hat{\kappa}$ can be diagonalized in the frame of the local magnetic field line. When the magnetic field is assumed to point in the z-direction $\mathbf{B} = Be_z$, the diffusion tensor reads $\hat{\kappa} = \text{diag}(\kappa_\perp, \kappa_\perp, \kappa_\parallel)$. The details of the assumed diffusion tensor are given in Section 3.1. The last term $S(\mathbf{r}, E, t)$ describes the sources and sinks of CRs, which are described in Section 3.2.

The term dE/dt quantifies the energy loss of CRs due to the interaction with the interstellar medium (ISM). In this process, charged and neutral pions are produced, where the π^0 decay into two photons. We use the hadronic interaction module presented in Hoerbe et al. (2020), which is based on the parameterization of the differential cross section in Kelner et al. (2006).

We solve the transport equation using the method of stochastic differential equations (SDEs) as implemented in the public transport code CRPropa3.2 (Batista et al. 2016; Merten et al. 2017; Batista et al. 2022). We calculate the steady-state solution following the approach in Merten et al. (2017). Details about the setup are given in Section 3.3.

3.1. Diffusion Tensor

In general, the diffusive transport of CRs is anisotropic with respect to the local magnetic field line. This fact, originally discussed for the transport of CRs in the heliospheric magnetic field (Jokipii 1966) and subsequently refined (e.g., Effenberger et al. 2012a; Shalchi 2021) as well as quantified (e.g., Reichherzer et al. 2022a), has in recent years also been acknowledged for their Galactic transport (e.g., Effenberger
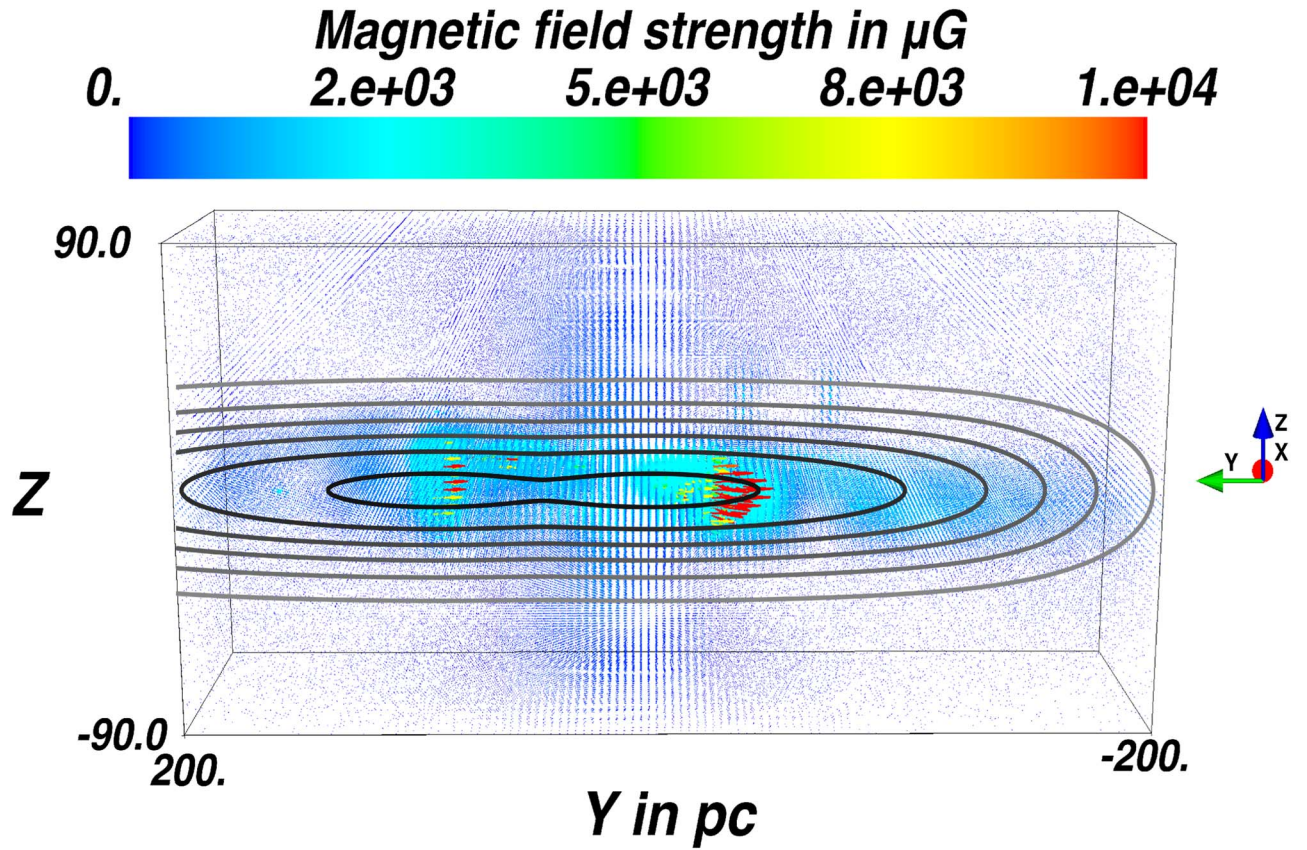
Figure 2. Superposition of the 3D magnetic field configuration from Guenduez et al. (2020; colored arrows) and the contours of the column density of the adapted gas distribution from Ferrière et al. (2007; gray lines).
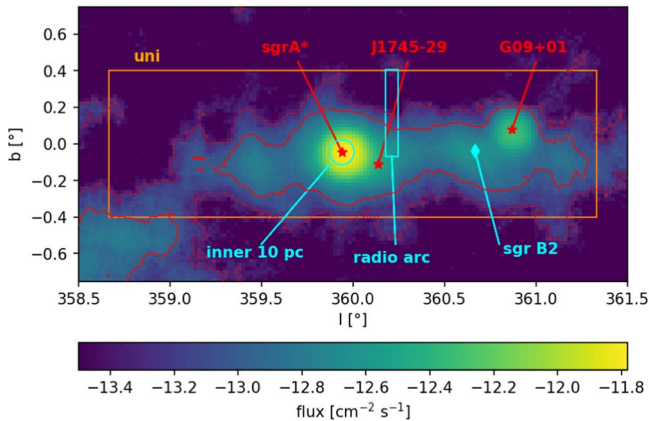

Figure 3. The VHE γ-ray flux from the CMZ observed by H.E.S.S. in Abdalla et al. (2018). The red lines show the contour for $\Phi = 10^{-13} \mathrm{cm}^{-2} \mathrm{s}^{-1}$ (solid red) and $\Phi = 5 \times 10^{-14} \mathrm{cm}^{-2} \mathrm{s}^{-1}$ (dashed red). The three red stars indicate the position of CR sources. The orange box indicates the simulation volume at $x = 0$. In cyan, we plot the three most important magnetic field components (the inner 10 pc structure, the radio arc, and the molecular cloud sgr B2).

et al. 2012b; Cerri et al. 2017, and references therein). This anisotropy is described by the diffusion tensor $\hat{\kappa}$ in the transport equation (Equation (3)).

To quantify the anisotropy, the ratio $\epsilon = \kappa_\perp / \kappa_\parallel$ of the diffusion coefficient perpendicular to the magnetic field line ($\kappa_\perp$) and along it ($\kappa_\parallel$) is used. In this work, we consider five different values ($\epsilon = 10^{-3}$, 10^{-2}, 0.1, 0.3, and 1) that reach from nearly purely parallel transport to isotropic diffusion. The value of this anisotropy should depend on the local turbulence

and can vary spatially (Reichherzer et al. 2020, 2022a, 2022b), but it is not known for the GC. Therefore, we test different fixed values to show the impact of this anisotropy parameter.

The energy scaling for the diffusion coefficients is taken from quasi-linear theory, and we normalize the parallel coefficient to match the observed value at Earth. With this, the parallel diffusion coefficient reads

$$\kappa_\parallel(E) = 6.1 \times 10^{24} \, \frac{\mathrm{m}^2}{\mathrm{s}} \cdot \left(\frac{E}{4 \, \mathrm{GeV}} \right)^{\frac{1}{3}}, \qquad (4)$$

using the particle energy E.

3.2. Sources

As the origin of CRs is not clear, we test two different scenarios for the spatial source distribution:

[3sr] The first source scenario considers the three observed γ-ray point sources as observed by H.E.S.S. They are (1) the central source Sgr A* (also called HESS J1745-290), (2) the supernova remnant G0.9+01, and (3) the pulsar HESS J1746-28. In this scenario, the contribution of the individual sources to the total CR luminosity is based on the γ-ray observation in Abdalla et al. (2018). This corresponds to a fraction of $f_{\mathrm{sgrA}} = 0.72$, $f_{\mathrm{G0.9}} = 0.22$, and $f_{\mathrm{J1746}} = 0.06$. A comparison between the source positions in this work and those used in Scherer et al. (2022) is given in Appendix A.

[uni] In the second source scenario, the full simulation volume is filled by a homogeneous CR source. This distribution

could correspond to a CR population that is accelerated outside the GC region and diffused into the CMZ a long time ago.

An overview of the source positions is indicated in Figure 3 by the red stars for the [3sr] scenario and by the orange rectangle for the [uni] source scenario.

In this work, we restrict our model to only contain protons. These are injected with a flat power-law spectrum $dN/dE|_{\text{sim}} \sim E^{-1}$ to ensure equal statistics in each logarithmic energy bin. In the post-processing of the simulation data, the source spectrum is reweighted to a power law $dN/dE|_s \sim E^{-\alpha_s}$ by assigning a weight

$$w_i = \frac{E_i^{\alpha_s - 1}}{\sum_i E_i^{\alpha_s - 1}} \qquad (5)$$

to each pseudo-particle, which is called candidate in CRPropa, as presented in Merten et al. (2017).

3.3. CRPropa Configuration

The simulation volume is a paraxial box of the size $200 \times 400 \times 120$ pc^3 centered on Sgr A*. For each source configuration and anisotropy parameter, a set of 50 simulations with $N_{\text{sim}} = 10^5$ primary CRs is performed. This splitting is necessary to keep the simulation time per run as well as the amount of data managable.[5]

The details of the used modules for the simulations are summarized in Table 1. The output contains all created γ-rays directly after their production. No propagation and corresponding absorption of γ-rays is taken into account. To realize this, we use the `DetectAll` observer and set a veto for nucleons.

The `DiffusionSDE` module (see Merten et al. 2017, for details) is used to calculate the solution of the transport equation. We use an adaptive step size with a precision of $P = 10^{-3}$. The diffusion tensor is described in Section 3.1. To speed up the simulation in the case of isotropic diffusion, we use a uniform magnetic field in the z-direction. In this case, the transport does not depend on the magnetic field configuration, but the adaptive step-size method would lower the steps to resolve the curvature of the magnetic field.

We limit the simulation to primary particles with a minimum energy of $E_{\text{min}} = 1$ TeV and a maximum simulation time[6] of $T_{\text{max}} = 500$ kpc c^{-1}. Moreover, all particles reaching the boundary of the simulation volume are lost.

3.4. Post-processing

After a simulation, all produced γ-rays are binned and reweighted according to the primary energy. This is done for different power-law indices α_s of the source emission. We test $1 \leqslant \alpha_s \leqslant 3$ with steps of $\Delta \alpha_s = 0.1$. The data are binned in longitude, latitude, and energy. In the first step, the binning is made in a much finer resolution than the current generation of imaging air Cherenkov telescopes (IACTs) can resolve. We use an angular binning of $\Delta l = 0°.016$ and $\Delta b = 0°.01$ to ensure enough statistics in each bin. The resolution effects of the

---

[5] This corresponds to ~600 CPU-h computation time and ~2 GB data output per run.
[6] The maximum simulation time is chosen to be much longer than the typical time a pseudo-particle spends in the simulation volume. In Appendix B we show that the particles leave the simulation volume earlier.

observation are later taken into account by smearing the results. This allows us to compare the data for future telescopes such as the upcoming CTA, which will have a two to three times better resolution (Cherenkov Telescope Array Consortium 2019). The energy binning is made in the same ranges as in the H.E.S.S. analysis (Abdalla et al. 2018).

4. Results

4.1. Synthetic Count Maps

Using the produced photons in our simulation, we create synthetic γ-ray maps by calculating weighted histograms of the longitudinal and latitudinal positions. The weighting takes the injection spectrum $dN/dE|_s \sim E^{-\alpha_s}$ into account. The resulting synthetic count maps for a source index $\alpha_s = 2.0$ are shown in Figure 4. In general, the maps do not change significantly for different source spectra. To compare our simulation with the observations by H.E.S.S., we apply a Gaussian smearing of $\sigma = 0°.077$, which is the 68% containment radius of the point-spread function (Abdalla et al. 2018). Appendix C contains the same count maps for the raw data without smearing.

In the case of strong parallel diffusion ($\epsilon = 0.001$), the CRs mainly follow the magnetic field lines. This leads to a stronger confinement of CRs in the MCs around Sgr A* and Sgr B2. Therefore, the γ-ray production is also centered near the sources/MCs. For the [3sr] source scenario, the emission around Sgr A* is stronger because the two sources close by emit more CRs. The emission in Sgr B2 shows the direction of the local field line where the CRs diffuse. By increasing perpendicular diffusion, the point-like emission is smeared out. The production of γ-rays at higher latitudes becomes more likely, and the distribution across the plane is spread out. In the extreme case of isotropic diffusion ($\epsilon = 1$), the point source G0.9 is barely visible and is hidden by the large-scale diffuse emission.

The γ-ray maps for the [uni] source injection show an extended disk for all anisotropies. This is expected due to the extended source distribution. Although the sources are distributed homogeneously, a concentration of produced photons around Sgr A* and Sgr B2 is visible. This effect is mainly caused by the stronger magnetic fields in these regions. As these fields are much more twisted, the confinement of CRs is more efficient, which also leads to a higher γ-ray production rate. Especially in the parallel diffusion-dominated case ($\epsilon = 10^{-3}$), the strongest emission is centered in Sgr B2. For the [uni] source injection, the increasing isotropy leads to a wider spread of γ-rays in latitude, while no clear difference between the longitudinal profiles is visible. Only in the case of isotropic diffusion are the peaks of Sgr A* and Sgr B2 no longer visible because this scenario does not depend on the magnetic field configuration.

4.2. Count Profiles

To quantify the difference between the distribution of photons, we compare our calculated γ-ray maps with the latitudinal and longitudinal profile presented by H.E.S.S. (see Figure 4 of Abdalla et al. (2018)). Analogously to the H.E.S.S. data analysis, all γ-rays in a latitudinal (longitudinal) window of $|b| \leqslant 0°.3$ ($|l| \leqslant 0°.5$) are collected. The profiles are calculated on a much finer binning ($\Delta l = 0°.016$ and $\Delta b = 0°.01$) and are smeared with the H.E.S.S. resolution of $\sigma = 0°.077$. The simulation data are normalized to match the maximum counts

Table 1
CRPropa Modules Used for the Simulation and Their Input Parameters

module	Parameter	Value
Magnetic Field and Propagation		
CMZField	Subcomponents	True
DiffusionSDE	Precision	$P = 10^{-3}$
	Minstep	$s_{min} = 10^{-3}$ pc
	Maxstep	$s_{max} = 10$ pc
	Anisotropy	$\epsilon \in \{10^{-3}, 10^{-2}, 0.1, 0.3, 1\}$
Observer and Output		
HDF5Output	Enabled columns	TrajectoryLength
		Position (source and current)
		Energy (source and current)
		Serial number
Observer	Particle veto	Nucleus, electron, neutrino
	Observer feature	ObserverDetectAll
Boundary and Break Condition		
MaximumTrajectoryLength	Maximum time	$T_{max} = 500$ kpc c^{-1}
MinimumEnergy	Minimum energy	$E_{min} = 1$ TeV
ParaxialBox	Origin	$o = (-100, -200, -60)$ pc
	Size	$s = (200, 400, 120)$ pc
ObserverSurface	Surface	Paraxial box as defined before.
Source		
SourceParticleType	Particle id	Proton (1000010010)
SourceIsotropicEmission		
SourceMultiplePositions	Positions	Sgr A* : $r = (0, 8.9, -6.8)$ pc
		J1746: $r = (0, -20.77, -16.32)$ pc
		G0.9+01: $r = (0, -129.08, 11.87)$ pc
or SourceUniformBox	Origin/size	o and s as above

Note. Module parameters not mentioned are kept at their default values.

of the latitudinal profile for $b = -0°.054$, which is the middle of its peak.

In Figure 5 we show the profiles for a source injection with a power law of $dN/dE|_s \sim E^{-2}$. The difference for varying the power-law slope α_s is shown in Appendix D. To estimate the agreement between the data and the simulation, the reduced χ^2

$$\chi^2_{red} = \frac{1}{n-1} \sum_{i=1}^{n} \frac{(c_i^{(obs)} - c_i^{(sim)})^2}{\sigma_i^2} \qquad (6)$$

is calculated. Here, c_i is the observed or simulated number of counts, σ_i is the observational uncertainty, and n is the total number of data points.

The latitudinal profiles for both source scenarios show a much too thin disk for high anisotropies of the diffusion tensor ($\epsilon = 0.001$ or $\epsilon = 0.01$). For the [uni] source model, the latitudinal profile is matched best using $\epsilon = 0.1$, while the [3sr] model prefers $\epsilon = 0.3$. In both source scenarios, the anisotropic diffusion is favored over the isotropic case ($\epsilon = 1$), however.

In contrast to the latitudinal profile, where both source scenarios show the same shape, clear differences are visible in the longitudinal profiles (left column of Figure 5). For the lowest anisotropy, the differences are strongest. The [3sr] model peaks considerably around the positions of the sources, and there is nearly no γ-ray production farther away. This is expected due to the strong confinement of CRs in the local environment of the sources. The [uni] model shows a nearly

smooth distribution over the full range. Only at the position $l = 0°.657$ is a maximum visible. This can be explained by the strong magnetic field of the MC Sgr B2. With stronger perpendicular diffusion, the peak of the [3sr] model is broader. For the [uni] source model, the trend is the opposite. In the case of stronger perpendicular diffusion (up to $\epsilon = 0.1$), the longitudinal profile becomes higher around Sgr A* , while the peak at Sgr B2 is spread out. This shift of the peaks in the γ-ray distribution might result from the small-scale structure of the magnetic field. Especially the position of the MCs and NTFs along the line of sight has a strong impact on the confinement of CRs. Overall, the strongest impact on the γ-ray distribution by the small-scale magnetic field is given by the MC sgr B2 and the field around Sgr A* . These components are highlighted in Figure 3.

A comparison between the χ^2_{red} values depending on the anisotropy of the diffusion tensor is shown in Figure 6. In the latitudinal comparison, the χ^2_{red} is comparable for all anisotropies $\epsilon \gtrsim 0.1$ and both source distributions. This is expected due to the fixed normalization of the count rate, and only the width of the distribution can change with the anisotropy.

Comparing the longitudinal profiles offers a better distinction between the source models and anisotropies because the normalization follows from the latitudinal profile. Taking only the longitude into account, the best agreement to the data is
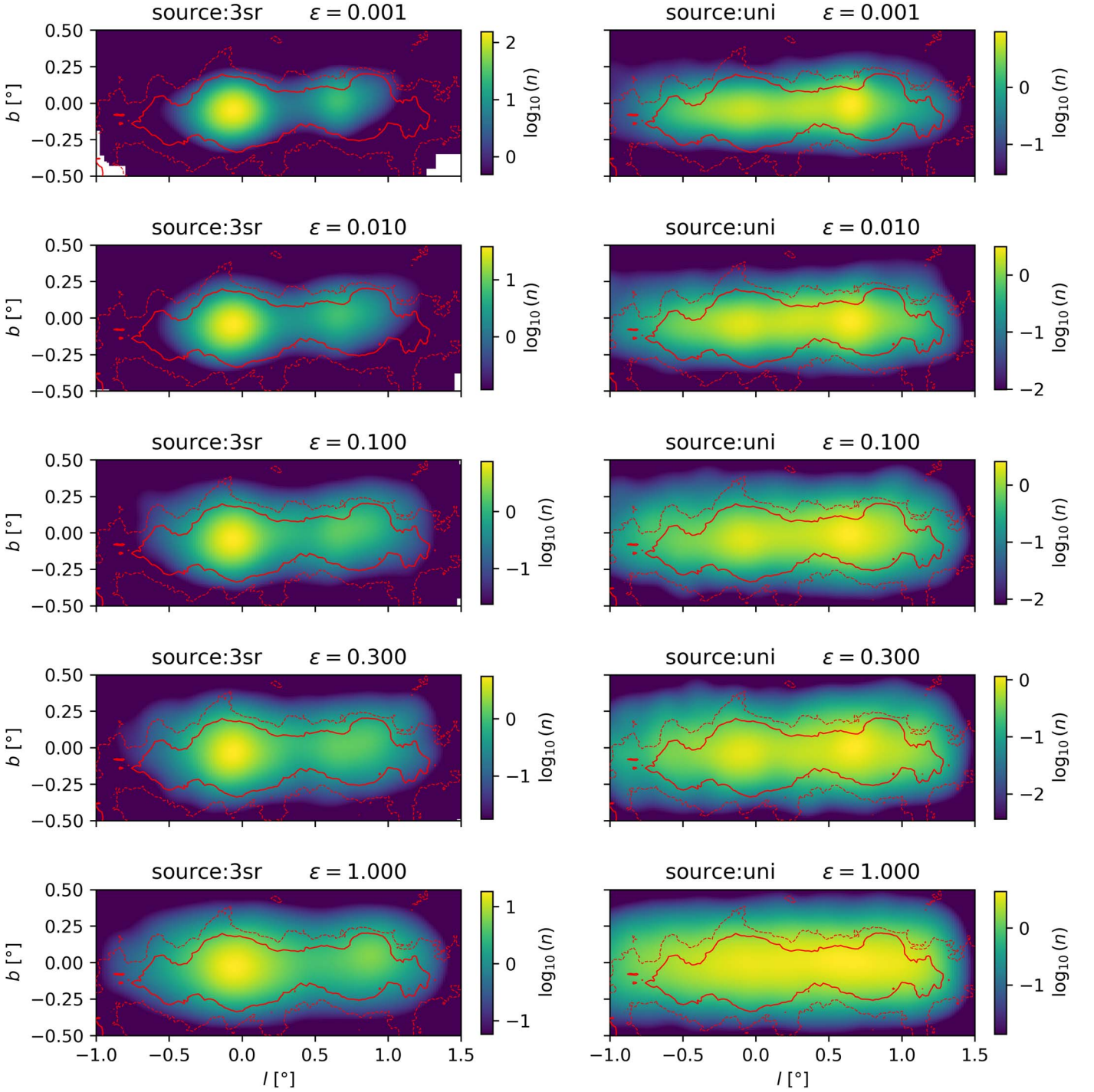
Figure 4. Synthetic γ-ray maps for a source injection with $\alpha_s = 2.0$. The first column shows the [3sr] source distribution, and the second column shows the [uni] injection scenario. The row denotes the anisotropy parameter $\epsilon \in \{0.001, 0.01, 0.1, 0.3, \text{and } 1\}$. The thin red lines show the contours of the observed flux by HESS (H. E. S. S. Collaboration et al. 2018) for $\Phi = 5 \cdot 10^{-14}$ cm^{-2} s^{-1} (dashed) and $\Phi = 10^{-13}$ cm^{-2} s^{-1} (solid).

Table 2
Best-fit Parameter for the Minimum χ^2_{red} Shown in Figure 8

Source	χ^2_{red}	ϵ	α_s	$\log_{10}(\Phi_0[\text{TeV cm}^{-2}\text{s}^{-1}])$	α	E_c [TeV]
[3sr]	3.23	0.3	1.9	-11.705 ± 0.022	2.219 ± 0.028	...
	3.65	0.1	2.0	-11.692 ± 0.014	2.21 ± 0.03	79 ± 21
[uni]	3.23	0.001	1.9	-11.702 ± 0.019	2.233 ± 0.024	...
	3.37	0.1	2.0	-11.695 ± 0.008	2.250 ± 0.016	307 ± 169

Note. For both spatial models, the first row corresponds to the power-law fit (Equation (7)), and the second row corresponds to the cutoff fit (Equation (8)).
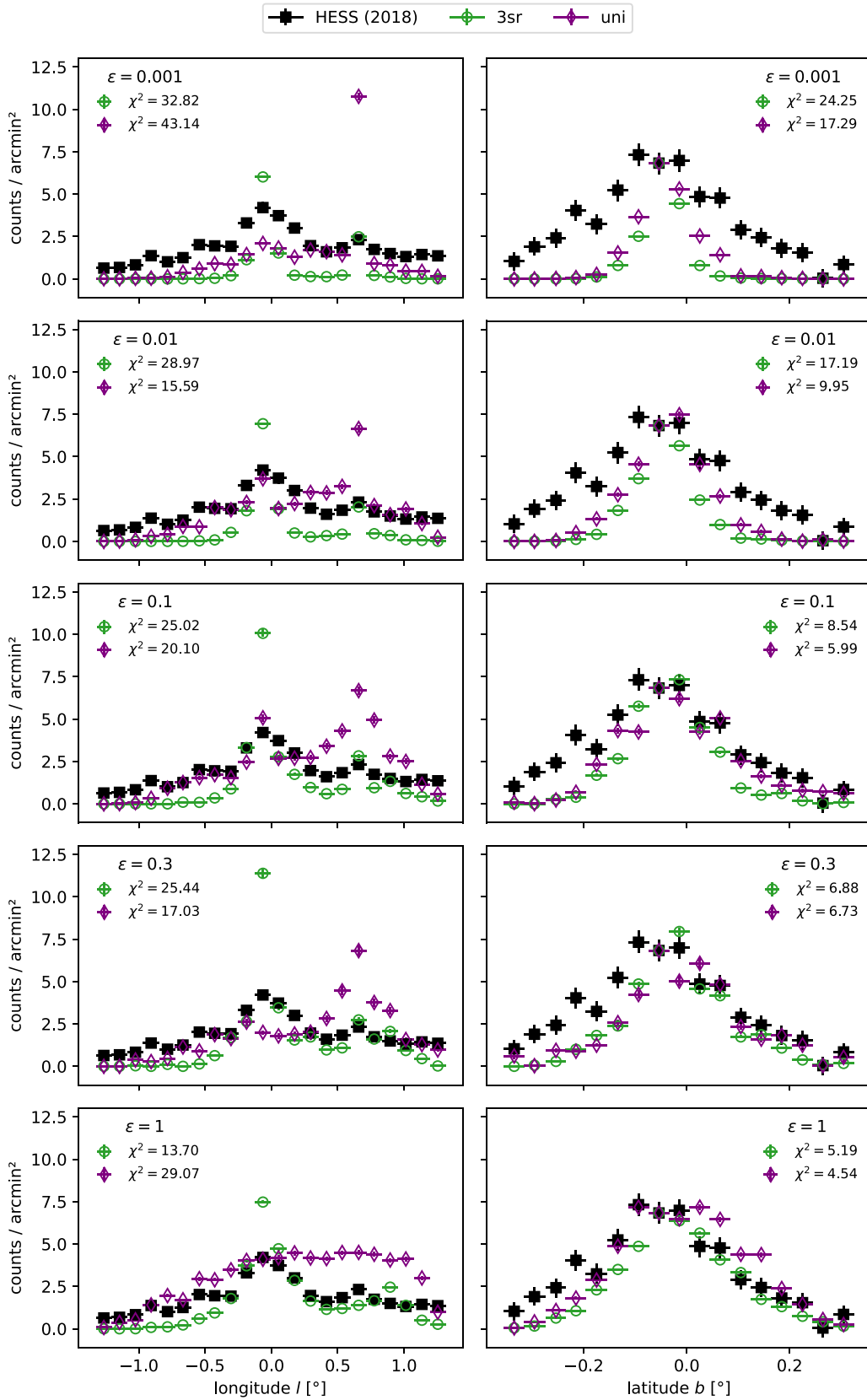
6

Figure 5. Profiles of the γ-ray distribution along the longitude (left column) and latitude (right column). The row denotes the anisotropy parameter.

reached for the [3sr] source distribution assuming isotropic diffusion ($\epsilon = 1$), although it still overshoots the height of the central peak. All [uni] models overpredict the peak at Sgr B2 and underpredict the peak at Sgr A*, and they can be ruled out.

4.3. Spectra

In addition to the angular distribution of the γ-ray flux, the spectral energy distribution (SED) is also measured by H.E.S.S.
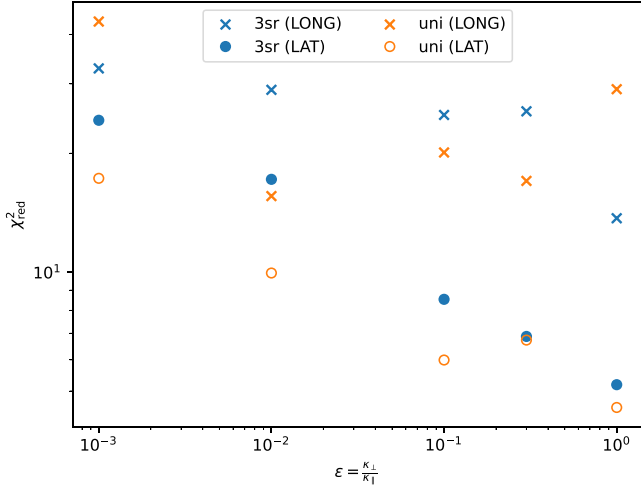
Figure 6. Reduced χ^2 values to quantify the difference between the observed count profiles and the simulation (compare Figure 5).

Figure 7. Example SED for the [3sr] source distribution and $\epsilon = 0.1$. Three different injection slopes α_s are shown.

(Abramowski et al. 2016), MAGIC (Acciari et al. 2020), and VERITAS (Adams et al. 2021). For this analysis, we consider different slopes of the CR injection spectrum $dN/dE|_s \sim E^{-\alpha_s}$. Indices in the range $1 \leqslant \alpha_s \leqslant 3$ with steps of $\Delta\alpha_s = 0.1$ are tested. For all configurations (source distribution, anisotropy of the diffusion tensor, and source-injection index) we bin the simulation data according to the H.E.S.S. observation, as they provide the finest energy resolution. The simulated SED is fit with a power law,

$$\Phi = \frac{dN}{dE} = \Phi_0 \left(\frac{E}{1 \text{ TeV}} \right)^{-\alpha}, \qquad (7)$$

where Φ_0 is the normalization at 1 TeV, and α is the spectral index and a power law with an exponential cutoff,

$$\Phi = \Phi_0 \left(\frac{E}{1 \text{ TeV}} \right)^{-\alpha} \exp \left\{ -\frac{E}{E_c} \right\}, \qquad (8)$$

with the cutoff energy E_c. The simulations in both cases allow for a free normalization Φ_0. Therefore, we choose the normalization to minimize the χ^2 difference between the fit and the observed data.

In Figure 7, the SED is shown for the injection slope of $\alpha_s = 1.7$ (orange), $\alpha_s = 2.0$ (green), and $\alpha_s = 2.3$ (purple) assuming the [3sr] spatial distribution and an anisotropy parameter of $\epsilon = 0.1$. We also show the observation by H.E.S.S. (Abramowski et al. 2016; red square), MAGIC (Acciari et al. 2020; blue diamond), and VERITAS (Adams et al. 2021; cyan triangle).

The results for the minimized χ^2 based on the different injection slopes is shown in Figure 8. All cases lead to the best fit for an injection slope $\alpha_s \approx 2$, while the pure power-law fit requires a slightly harder injection spectrum. The parameters for the best fits are summarized in Table 2. No clear preference for the anisotropy parameter can be found for the SED fitting.

Due to the hadronic nature of the γ-ray production, we also expect a neutrino component. When the absorption of γ-rays is neglected, the all flavor neutrino flux can be approximated as $\Phi_{\nu,\text{tot}}(E_\nu) = 6\,\Phi_\gamma(E_\nu/2)$ (Becker Tjus & Merten 2020). Using the neutrino flux Φ_ν and the effective area A_{eff} of the neutrino detection from the Galactic plane (Abbasi et al. 2023), we can calculate the expected number of neutrinos within the 10 yr of IceCube data as
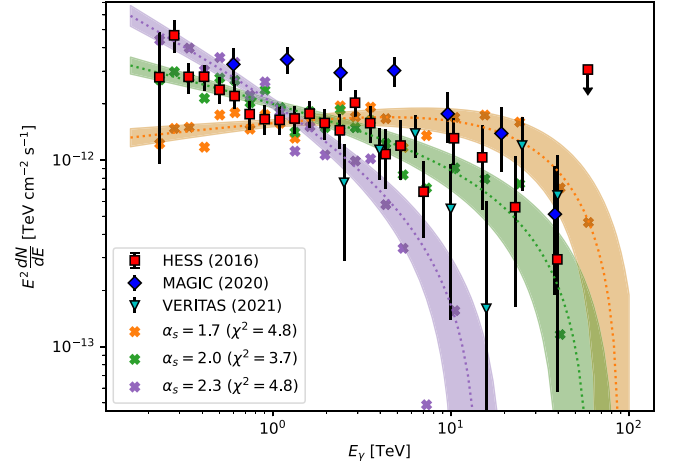
$$N_\nu = \Delta t_{\text{obs}} \int \Phi_\nu(E) \, A_{\text{eff}}(E) \, dE. \qquad (9)$$

In the most optimistic scenario, which is a power-law-like emission from the [3sr] source distribution, the expected number of neutrinos is $N_\nu = 0.016$. This makes the observation of the CMZ as a neutrino point source within the Galactic plane very unlikely.

4.4. Source Luminosity

To estimate the required energy budget of the CR sources within the CMZ, we ran a set of smaller simulations with $N_{\text{sim}} = 10^4$ for each anisotropy ϵ. In addition to the simulation setup described in Section 3.3, an output of all injected primary protons was added.

The absolute normalization of the simulated CR and γ-ray fluxes can be achieved by assigning weights to candidates based on the luminosity at the source L_{src} and the distance to the observer r_{obs} (see, e.g., Appendix A in Eichmann & Kachelrieß, 2023). In our case, considering only one source species and assuming all photons to be emitted at $r_{\text{obs}} = 8.5$ kpc, the normalization factor between the simulated flux J (in unit particles/TeV) and the physical flux Φ reduces to a constant factor and is independent of the observed particle species.

To estimate the normalization factor

$$f^\gamma = \frac{J_\gamma(1 \text{ TeV})}{\Phi_\gamma(1 \text{ TeV})}, \qquad (10)$$

we perform the same fitting as described in Section 4.3 on the smaller test setup assuming a source injection with $\alpha_s = 2.0$. Applying the same factor to the simulated proton spectrum at the source J_p, we can estimate total CR luminosity as

$$L_p(E \geqslant 10 \text{ TeV}) \approx \int_{10 \text{ TeV}}^{1 \text{ PeV}} dE_p \, E_p \, J_p(E_p) \, f^\gamma \, 4\pi r_{\text{obs}}^2. \qquad (11)$$

The resulting source luminosity, depending on the anisotropy and the type of the performed fit, is shown in Figure 9. The source luminosity depends only slightly on the assumed anisotropy of the diffusion tensor and is within the required
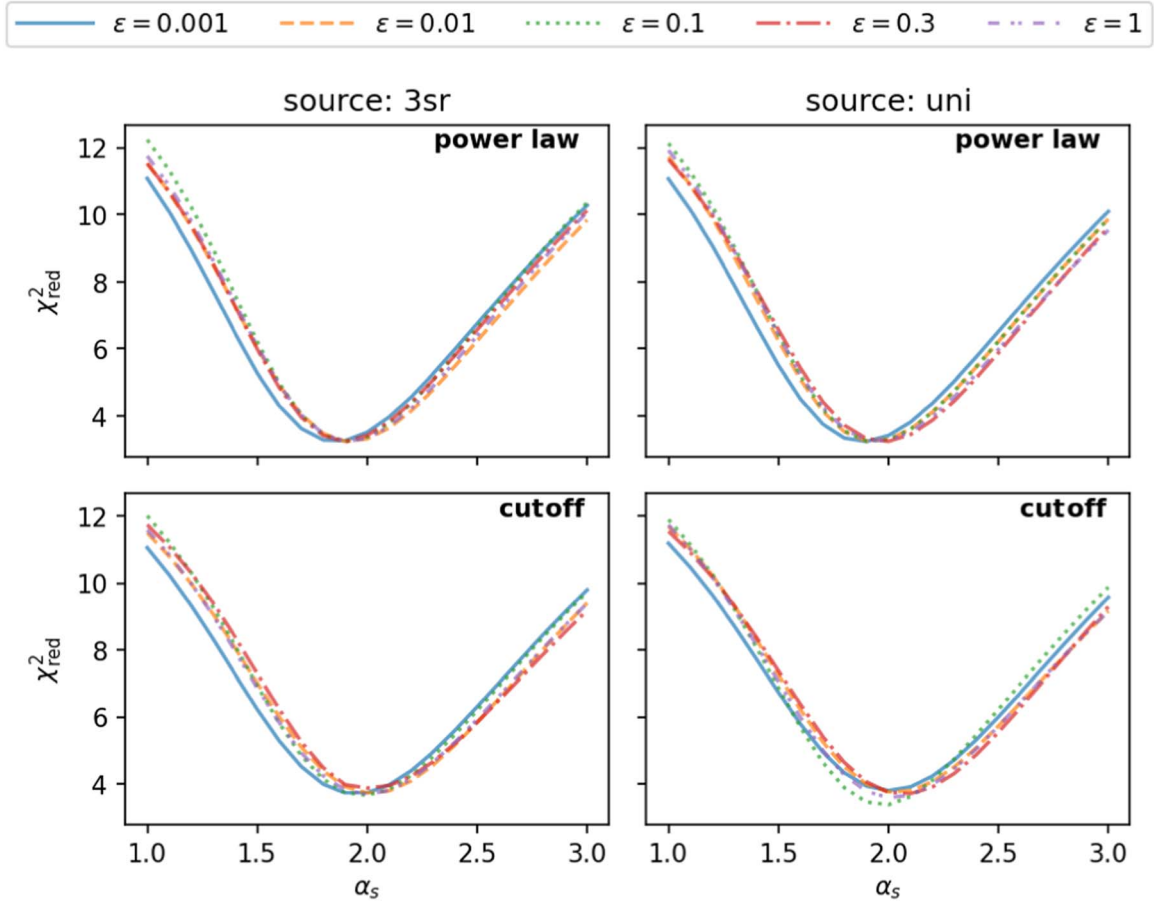
Figure 8. χ^2 difference between the fitted SED and the observation depending on the source-injection slope. The column indicates the spatial source distribution (left: [3sr] , and right: [uni]), and the row indicates the fitting function (upper: power law (Equation (7)), lower: power law with cutoff (Equation (8))). The line color and style denote different anisotropies of the diffusion tensor.
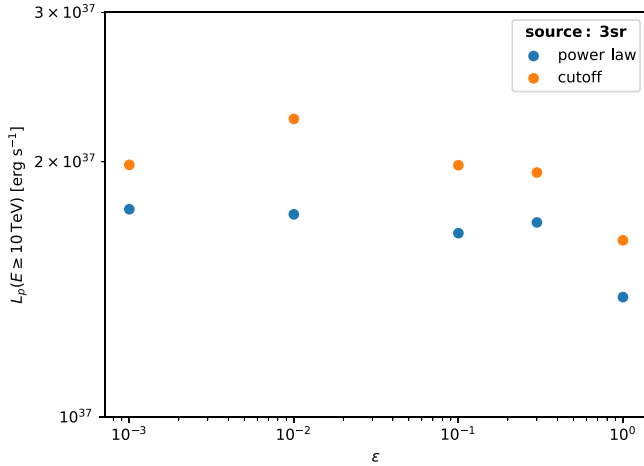

Figure 9. Estimated source luminosity in the [3sr] source scenario, assuming $\alpha_s = 2.0$

acceleration rate of 10^{37}–10^{38} erg s^{-1}, as claimed by H.E.S.S. (Abramowski et al. 2016).

5. Summary and Conclusion

Building a realistic 3D model of the CR transport inside the CMZ requires detailed knowledge of the astrophysical environment, i.e., the gas distribution, the magnetic field configuration, and the source positions.

In our work, we used the 3D gas distribution from Ferrière et al. (2007). We adjusted the exponential scale height to $H_c = 30$ pc to match the observed thickness of the γ-ray emission, which is close to the upper limit of the observational uncertainties. All transport scenarios using the original thickness would lead to a thinner disk, as the maximum width of the γ-ray distribution is given by the density distribution. Increasing the scale height to even higher values would also allow the more anisotropic diffusion scenarios to match the latitudinal profile, but the longitudinal behavior would not be affected.

The anisotropy of the diffusion tensor $\epsilon = \kappa_\perp / \kappa_\parallel$, defined as the ratio of the diffusion perpendicular and parallel to the magnetic field line, is constrained by the observation of the longitudinal and latitudinal profiles and the SED of the γ-ray emission. The measurements by the H.E.S.S. telescopes (Abdalla et al. 2018) indicate a nearly isotropic diffusion of CRs, while in the SED fitting, no clear preference can be seen. The required source luminosity is reasonable within the range expected by Abramowski et al. (2016).

In this work, we tested two different source scenarios, three different point sources within the CMZ, and a global sea of old CRs from the Milky Way that diffuse into the CMZ. The distinction between the different source distributions and anisotropies is done best by comparing the longitudinal

profiles. In this case, the best agreement with the data could be achieved by the point-source scenario. Here, the smallest χ^2_{red} can be achieved. Only the position of the peak for positive longitudes is shifted slightly outward. The distribution underpredicts the outermost part. This might indicate a missing gas target in this range or a contribution from the CR sea.

In general, the large-scale observables could be reproduced with our 3D model of the CMZ, but some of the small-scale features such as the small enhancement at $l \lesssim -0°.5$ and the exact position of the peak around $l \sim 0°.7$ are still lacking. This is mainly due to the lack of substructures within the gas distribution, but a more refined magnetic field model would also be needed. In the outer part of the model, the transition between the dense CMZ gas and the thinner Galactic disk needs to be modeled more carefully.

This will become important with the upcoming next-generation telescopes such as the CTA, which will provide a lower angular resolution and a better sensitivity. It will allow us to distinguish between the contribution from different molecular clouds, and the improved statistic will enable us to test spectral differences between different regions within the CMZ.

Appendix A
Comparing Source Positions

In this section, the differences of the source positions used in this work from those used by Scherer et al. (2022) are shown. Scherer et al. (2022) focused on the emission from star clusters (the Nuclear Star Cluster [NSC], the Arches Cluster [AC], and the Quintuplet Cluster [QC]). Additionally, they introduce the source SgrA east as an impulsive source. The distances of NSC and sgrA east to our source SgrA* are much shorter than the resolution of H.E.S.S. Therefore, we do not expect a difference here.

The other clusters (AC and QC) are a possible source for CR acceleration, but are not observed in VHE γ-rays. Based on this, we use the identified γ-ray source HESS J1745-29 instead. In the outer part, Scherer et al. identified the supernova remnant sgrD as a contributing source. They discuss three G-objects as a
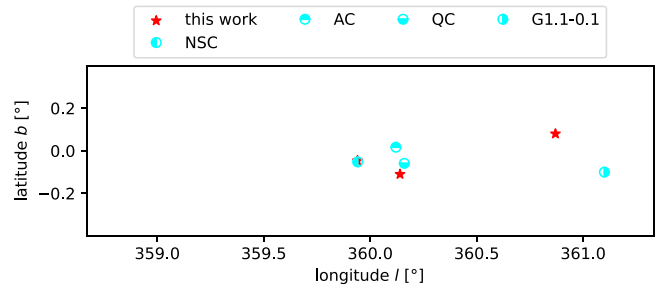

Figure 10. Comparison of the source positions in this work (red stars) to those used by Scherer et al. (2022; cyan circles).

possible source (G1.1-0.1, G1.0-0.2, and G0.9+0.1). They arbitrarily choose the middle one, G1.0-0.2, as the source, but only G0.9+0.1 is observed in VHE γ-rays. Therefore, we use this source.

In Figure 10, the different source positions from this work and Scherer et al. (2022) are shown.

Appendix B
Estimating the Maximum Simulation Time

To estimate the necessary total simulation time, we test the number of particles left in the simulation volume in steps of $\Delta t = 20 \frac{kpc}{c}$. This is done for all simulation setups with $N_{sim} = 10^4$ primaries.

In general, the escape time is shorter for a less anisotropic diffusion. In Figure 11, the fraction of particles in the simulation volume is shown as a function of time. Here, the cases with $\epsilon = 10^{-3}$ are chosen to show the longest residence time. In both cases, more than 99% of the particles left the volume before $t = 100 \frac{kpc}{c}$. Therefore, a total simulation time with $T_{max} = 500 \frac{kpc}{c}$ is even more conservative.
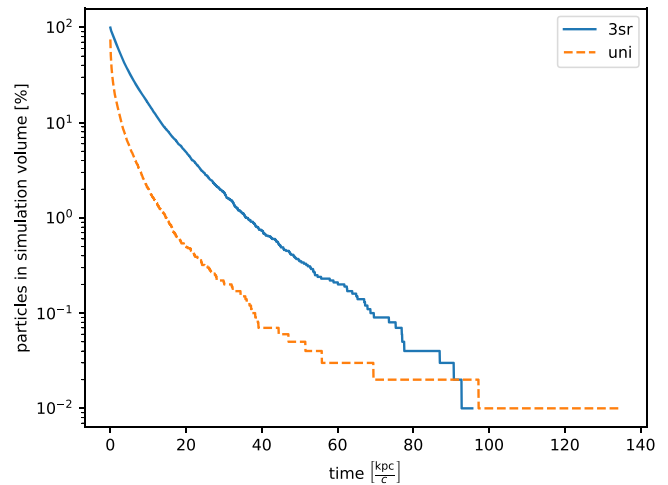

Figure 11. Number of particles left in the simulation volume.

Appendix C
Raw Data for 2D Count Maps

In Figure 12, the raw data for the synthetic γ-ray count maps are shown. The underlying binning uses $\Delta l = 0°016$ and $\Delta b = 0°01$. The simulation in principle allows for a finer binning, but the statistics in each bin decreases. The bin size is chosen to minimize the noise, but keep the small-scale structures visible.
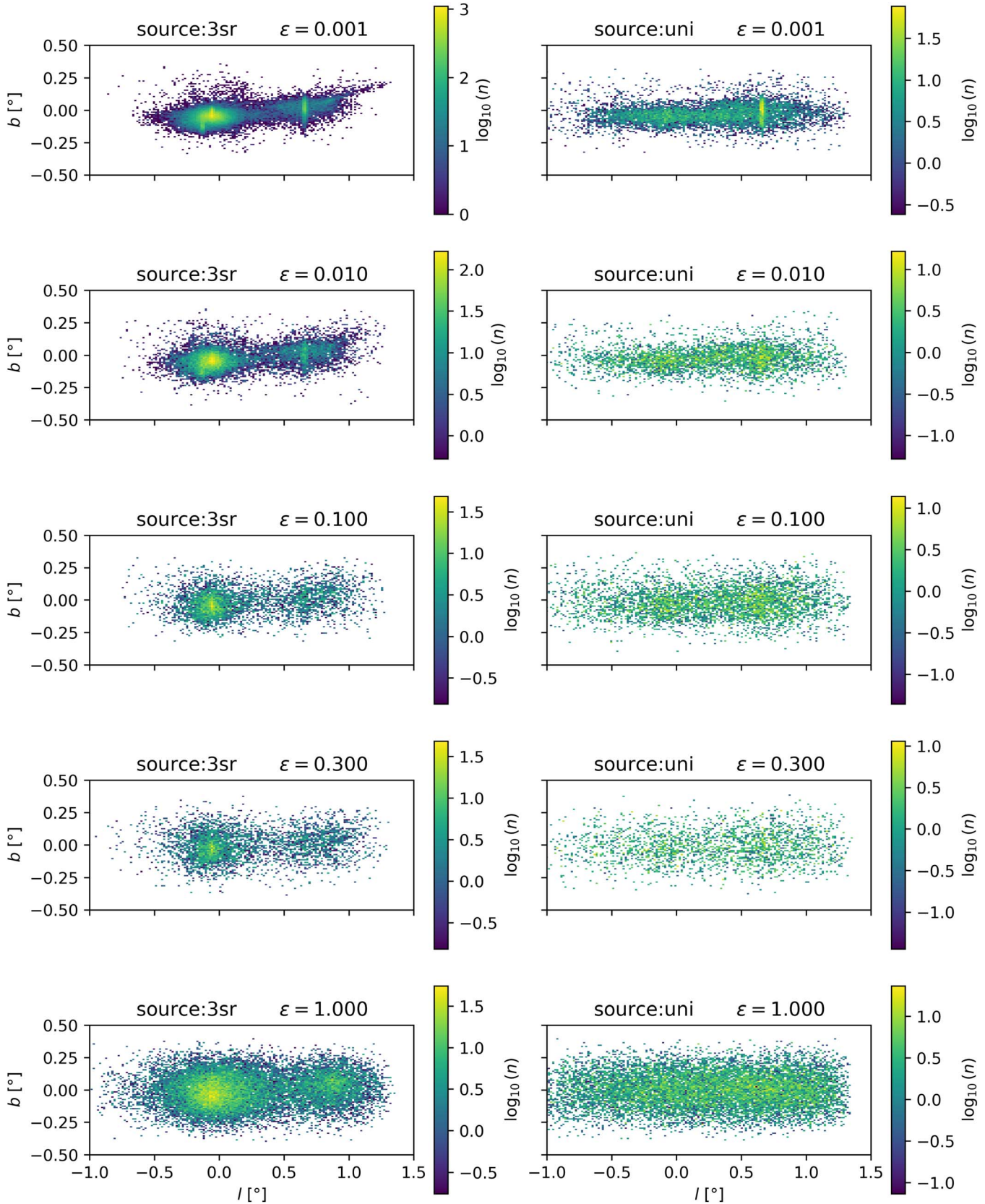

Figure 12. Synthetic γ-ray maps as shown in Figure 4, but without a smearing for a PSF.

In the case of strong parallel transport, the small-scale structures of the magnetic field can be seen. For both source distributions, the impact of the NTF called radio arc can bee seen. In the case of the [3sr] source distribution, smaller filaments in the region around Sgr A* are also visible.

For higher values of the isotropy parameter ϵ, this effect is smeared out. For $\epsilon = 0.01$, only the radio arc is visible for the [3sr] distribution by eye. In the other cases, no small-scale structure appears.

Appendix D
Impact of Source Spectra on the Count Profile

In Section 4.2, the impact of the anisotropy on the resulting count profiles is shown. This analysis was only performed for the case of a power-law injection with a slope $\alpha_s = 2$, which is consistent with the results from Section 4.3. In Figure 13, the dependence of the reduced χ^2 on the source injection index is shown. In general, no strong trend is observed. Only for the
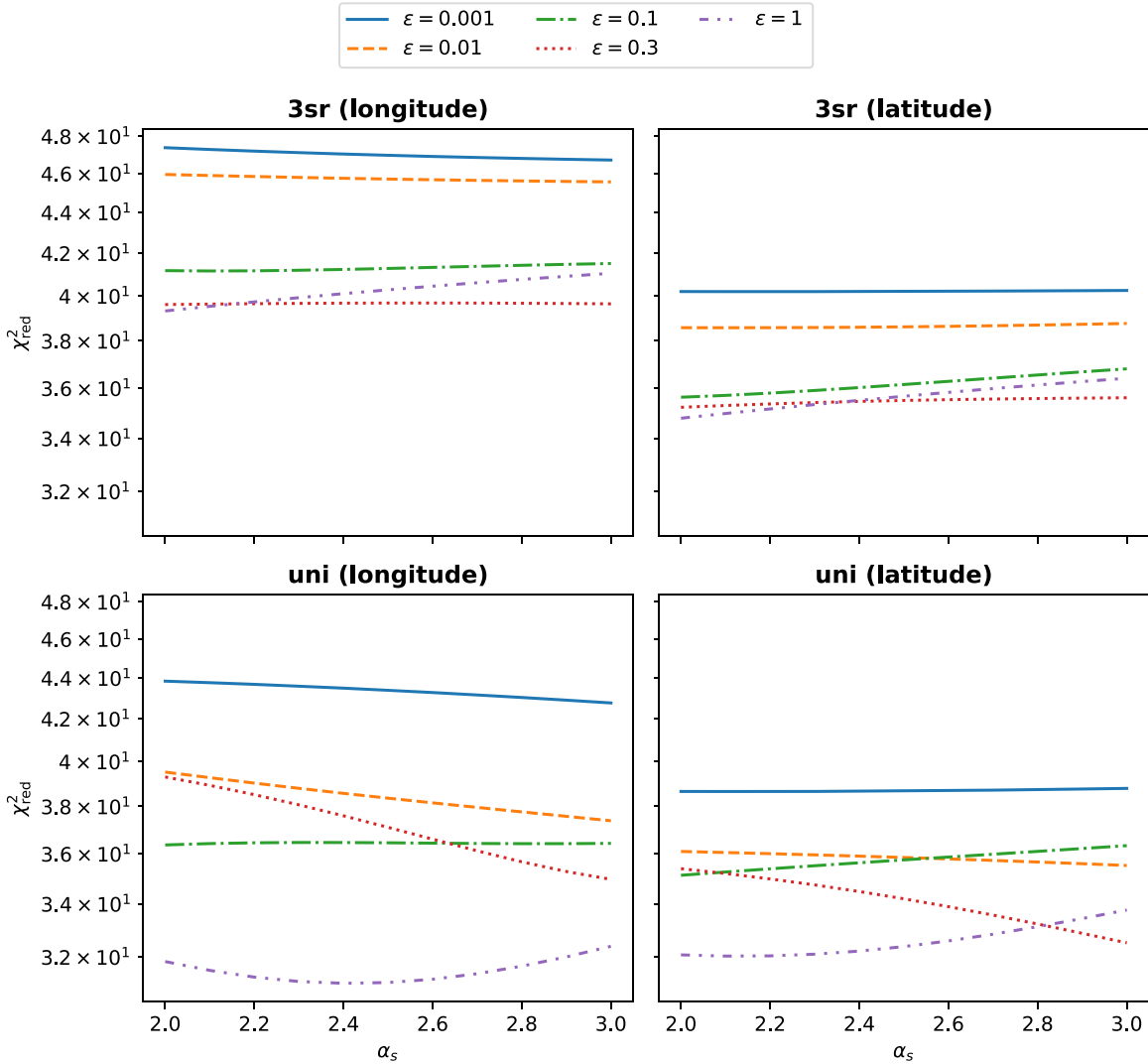

Figure 13. Impact of the source power-law index α_s on the reduced χ^2 difference between the simulation and the observed H.E.S.S.profile.

most extreme source indices $\alpha_s \geqslant 2.7$ are some changes in the preferred anisotropy seen. This steep injection scenario can be excluded from the SED fitting in Section 4.3, however.

The general statement in Section 4.2 does not change for a choice of $\alpha_s = 2.0$.

ORCID iDs

J. Dörner ● https://orcid.org/0000-0001-6692-6293
J. Becker Tjus ● https://orcid.org/0000-0002-1748-7367
P. S. Blomenkamp ● https://orcid.org/0000-0002-5032-5896
H. Fichtner ● https://orcid.org/0000-0002-9151-5127
A. Franckowiak ● https://orcid.org/0000-0002-5605-2219

References

Abbasi, R., Ackermann, M., Adams, J., et al. 2023, ApJ, 956, 20
Abdalla, H., Abramowski, A., Aharonian, F., et al. 2018, A&A, 612, A9
Abramowski, A., Aharonian, F., Benkhali, F. A., et al. 2016, Natur, 531, 476
Acciari, V. A., Ansoldi, S., Antonelli, L. A., et al. 2020, A&A, 642, A190
Ackermann, M., Ajello, M., Albert, A., et al. 2017, ApJ, 840, 43
Ackermann, M., Albert, A., Atwood, W. B., et al. 2014, ApJ, 793, 64
Adams, C. B., Benbow, W., Brill, A., et al. 2021, ApJ, 913, 115
Ajello, M., Albert, A., Atwood, W. B., et al. 2016, ApJ, 819, 44
Batista, R. A., Dundovic, A., Erdmann, M., et al. 2016, JCAP, 2016, 038
Batista, R. A., Tjus, J. B., Dörner, J., et al. 2022, JCAP, 2022, 035
Becker Tjus, J., & Merten, L. 2020, PhR, 872, 1
Cao, Z., Aharonian, F., An, Q., et al. 2023, PhRvL, 131, 151001
Cerri, S. S., Gaggero, D., Vittino, A., Evoli, C., & Grasso, D. 2017, JCAP, 2017, 019
Cherenkov Telescope Array Consortium 2019, Science with the Cherenkov Telescope Array (Singapore: World Scientific)
Daylan, T., Finkbeiner, D. P., Hooper, D., et al. 2016, PDU, 12, 1
Di Mauro, M. 2021, PhRvD, 103, 063029
Effenberger, F., Fichtner, H., Scherer, K., & Büsching, I. 2012b, A&A, 547, A120
Effenberger, F., Fichtner, H., Scherer, K., et al. 2012a, ApJ, 750, 108
Eichmann, B., & Kachelrieß, M. 2023, JCAP, 2023, 053
Ferrière, K., Gillard, W., & Jean, P. 2007, A&A, 467, 611
Finkbeiner, D. P. 2004, ApJ, 614, 186
Goodenough, L., & Hooper, D. 2009, arXiv:0910.2998
Guenduez, M., Becker Tjus, J., Ferrière, K., & Dettmar, R. J. 2020, A&A, 644, A71
Harris, C. R., Millman, K. J., van der Walt, S. J., et al. 2020, Natur, 585, 357
Henshaw, J. D., Barnes, A. T., Battersby, C., et al. 2023, in ASP Conf. Ser. 534, Protostars and Planets VII (San Francisco, CA: ASP), 83
H. E. S. S. Collaboration, Abdalla, H., Abramowski, A., et al. 2018, A&A, 612, A1
Heywood, I., Rammala, I., Camilo, F., et al. 2022, ApJ, 925, 165
Hoerbe, M. R., Morris, P. J., Cotter, G., & Becker Tjus, J. 2020, MNRAS, 496, 2885
Hunter, J. D. 2007, CSE, 9, 90
Jokipii, J. R. 1966, ApJ, 146, 480
Kelner, S. R., Aharonian, F. A., & Bugayov, V. V. 2006, PhRvD, 74, 034018
Merten, L., Becker Tjus, J., Fichtner, H., Eichmann, B., & Sigl, G. 2017, JCAP, 2017, 046
Pedlar, A., Anantharamaiah, K. R., Ekers, R. D., et al. 1989, ApJ, 342, 769
Pérez, F., & Granger, B. E. 2007, CSE, 9, 21
Planck Collaboration, Ade, P. A. R., Aghanim, N., et al. 2013, A&A, 554, A139
Reichherzer, P., Becker Tjus, J., Zweibel, E. G., Merten, L., & Pueschel, M. J. 2020, MNRAS, 498, 5051
Reichherzer, P., Becker Tjus, J., Zweibel, E. G., Merten, L., & Pueschel, M. J. 2022a, MNRAS, 514, 2658
Reichherzer, P., Merten, L., Dörner, J., et al. 2022b, SNAS, 4, 15
Rocklin, M. 2015, in Proc. of the 14th Python in Science Conf., ed. K. Huff & J. Bergstra, 126
Scherer, A., Cuadra, J., & Bauer, F. E. 2022, A&A, 659, A105
Scherer, A., Cuadra, J., & Bauer, F. E. 2023, A&A, 679, A114
Shalchi, A. 2021, ApJ, 923, 209
Sofue, Y. 2000, ApJ, 540, 224
Virtanen, P., Gommers, R., Oliphant, T. E., et al. 2020, NatMe, 17, 261